ADVANCED FUNCTIONAL MATERIALS

www.afm-journal.de

A Generic Soft Encapsulation Strategy for Stretchable Electronics

*Kan Li, Xu Cheng, Feng Zhu, Linze Li, Zhaoqian Xie, Haiwen Luan, Zhouheng Wang, Ziyao Ji, Heling Wang, Fei Liu, Yeguang Xue, Changqing Jiang, Xue Feng, Luming Li, John A. Rogers, Yonggang Huang, and Yihui Zhang**

Recent progress in stretchable forms of inorganic electronic systems has established a route to new classes of devices, with particularly unique capabilities in functional biointerfaces, because of their mechanical and geometrical compatibility with human tissues and organs. A reliable approach to physically and chemically protect the electronic components and interconnects is indispensable for practical applications. Although recent reports describe various options in soft, solid encapsulation, the development of approaches that do not significantly reduce the stretchability remains an area of continued focus. Herein, a generic, soft encapsulation strategy is reported, which is applicable to a wide range of stretchable interconnect designs, including those based on two-dimensional (2D) serpentine configurations, 2D fractal-inspired patterns, and 3D helical configurations. This strategy forms the encapsulation while the system is in a prestrained state, in contrast to the traditional approach that involves the strain-free configuration. A systematic comparison reveals that substantial enhancements (e.g., ≈6.0 times for 2D serpentine, ≈4.0 times for 2D fractal, and ≈2.6 times for 3D helical) in the stretchability can be achieved through use of the proposed strategy. Demonstrated applications in highly stretchable light-emitting diodes systems that can be mounted onto complex curvilinear surfaces illustrate the general capabilities in functional device systems.

1. Introduction

Rapid development of the technologies of stretchable electronics has enabled a diversity of mechanically compliant biointerfaces between rigid inorganic electronic components and soft biological tissues,[1–24] as a means to monitor health conditions and to execute certain therapies.[25–35] A majority of previous studies in this area focused on the development of materials designs and mechanics concepts to achieve a high degree of deformability, while maintaining high-performance functionality.[36–53] A reliable scheme for encapsulating stretchable electronics platforms is essential for practical applications, since a direct physical contact with the outside environment could result in failure of fragile device components and/or interconnects.[4,54] Despite the importance, relatively few studies focus on the development of encapsulation strategies with enhanced performance or robustness. Most approaches simply involve the application of soft elastomer encapsulants as a final step in the fabrication process.[55–60] For example, Vanfleteren's group[61–64] studied extensively the deformation behaviors and failure mechanisms of planar serpentine-shaped conductors encapsulated with polymers. For stretchable metallic interconnects with different bonding conditions (e.g., fully or partially bonded to the substrates), the solid encapsulant typically leads to a pronounced reduction in the elastic

K. Li, F. Zhu, Dr. Z. Xie, H. Luan, Dr. H. Wang, Y. Xue, Prof. Y. Huang
Department of Civil and Environmental Engineering
Mechanical Engineering, and Materials Science and Engineering
Center for Bio-Integrated Electronics
Northwestern University
Evanston, IL 60208, USA

X. Cheng, Z. Wang, Z. Ji, F. Liu, Prof. X. Feng, Prof. Y. Zhang
Center for Mechanics and Materials
and Center for Flexible Electronics Technology
AML
Department of Engineering Mechanics
Tsinghua University
Beijing 100084, P. R. China
E-mail: yihuizhang@tsinghua.edu.cn

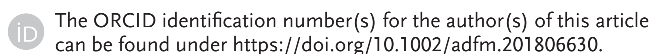
The ORCID identification number(s) for the author(s) of this article can be found under https://doi.org/10.1002/adfm.201806630.

DOI: 10.1002/adfm.201806630

F. Zhu
School of Logistics Engineering
Wuhan University of Technology
Wuhan 430063, P. R. China

L. Li, Prof. C. Jiang, Prof. L. Li
National Engineering Laboratory for Neuromodulation
School of Aerospace Engineering
Tsinghua University
Beijing 100084, P. R. China

Prof. J. A. Rogers
Departments of Materials Science and Engineering
Biomedical Engineering, Neurological Surgery, Chemistry,
Mechanical Engineering
Electrical Engineering and Computer Science
and Center for Bio-Integrated Electronics
Northwestern University
Evanston, IL 60208, USA

© 2019 WILEY-VCH Verlag GmbH & Co. KGaA, Weinheim

stretchability, due to constraints on the out-of-plane motions of the interconnects. Liquid encapsulation schemes[65,66] avoid this limitation, but they introduce leakage as a possible failure mode. A partially released encapsulation method[67] was proposed recently to improve the stretchability of 3D helical interconnects, which, however, could not be extended directly to 2D shaped interconnects (e.g., serpentine interconnects) that were widely exploited in stretchable electronic devices. Development of a generic solid encapsulation strategy that does not sacrifice stretchability remains a challenge.

Here, we report a two-stage sequence for introducing solid encapsulation materials on stretchable electronic systems, with wide applicability across the most advanced interconnect configurations, including 2D serpentine,[68–75] 2D fractal-inspired shapes,[65,76] and 3D helical coils.[67,77–80] This strategy forms the solid encapsulation while the electronic system is in a prestretched state, instead of the load-free state adopted in conventional strategies. Release of the prestretch after application of the encapsulation completes the process. In this manner, the constraints of the solid encapsulant on the interconnect deformations that occur under external loading can be relieved substantially, as demonstrated by both experiments and mechanics modeling. Quantitative studies based on finite element analysis (FEA) illustrate methods to optimize this two-stage encapsulating process to maximize the stretchability. By comparison to the conventional one-stage encapsulation strategy, this two-stage process increases the elastic stretchability, e.g., by factors of ≈6.0 for 2D serpentine interconnects, ≈4.0 for 2D fractal interconnects, and ≈2.6 for 3D helical interconnects. Highly stretchable collections of light-emitting diodes (LEDs) that be mounted onto complex curvilinear surfaces serve application examples.

2. A Two-Stage Soft Encapsulation Strategy

Figure 1a presents a schematic illustration of a two-stage encapsulating process for stretchable electronics constructed with 2D serpentine interconnects. During the first stage of the two-stage encapsulating process, the elastomeric substrate (E = 20 kPa; Ecoflex 00-30A/B, Smooth-on, USA) is prestretched to an encapsulating strain ($\varepsilon_{\text{encap}}$), at which the soft encapsulation layer (E = 3 kPa; Silbione 4717A/B, Bluestar Silicones, France) is added. In the second stage, the substrate is fully released to complete the encapsulation. In contrast, the conventional one-stage encapsulating process forms the solid encapsulation when the system is in a load-free state, without applying any prestretch (Figure 1b). Note that the 2D serpentine interconnects are selectively bonded to the substrate at the two ends before the encapsulation, such that the prestretch leads to a buckled 3D configuration through controlled bending and twisting deformations. Such a buckled 3D configuration plays an important role in enhancing the stretchability in the encapsulated condition, as elaborated subsequently.

Mechanics modeling based on 3D FEA (see the Experimental Section for details) allows quantitative evaluation of the two-stage encapsulation strategy. Consider, for example, serpentine interconnects consisting of polyimide (PI)/metal/PI multilayers, where PI layers (1.4 µm) serve as supports to mechanically protect the ultrathin metal layer (0.2 µm) from failure. Positioning the metal layer at the neutral mechanical plane of the sandwich design reduces the maximum strain in the metal during stretching, thereby increasing the overall stretchability. In the FEA, the elastic stretchability is defined as the overall dimensional change below which the structural deformations can recover completely. Considering that the elastic strain limit of PI (>8%)[81] is much larger than that of metal (e.g., Au, ≈0.25%), the elastic stretchability is typically limited by the metal layer. Figure 1c shows that the elastic stretchability (61%) of 2D serpentine interconnects with the two-stage encapsulation is more than six times higher than that (9%) with one-stage encapsulation. The substantial improvements of elastic stretchability follow from the distinct mechanisms of stress accumulation. For interconnects with one-stage encapsulation, the maximum Mises stresses in the metal layer increase rapidly and monotonically (Figure 1c), as the stretching proceeds, which limits the elastic stretchability. By comparison, the maximum Mises stresses in the interconnects with two-stage encapsulation decrease first to reach a local minimum as the applied strain reaches $\varepsilon_{\text{encap}}$, and then increases beyond $\varepsilon_{\text{encap}}$. This behavior is mainly attributed to predeformed interconnects that can accommodate an applied strain at least larger than $\varepsilon_{\text{encap}}$. The selection of a proper encapsulating strain ($\varepsilon_{\text{encap}}$) is essential in the design optimization, as shown in the next two sections.

Figure 1d–f presents the deformed configurations with Mises stress distributions for 2D serpentine interconnects stretched to the corresponding elastic limits, in which both the one-stage and two-stage encapsulating processes are taken into account. Distinct deformation mechanisms can be observed from such as comparison. In particular, the lateral buckling during the prestretching stage of two-stage encapsulating process leads to buckled 3D configurations. With solid encapsulation, such buckled 3D configurations can be unraveled more easily than 2D configurations that are entirely restricted to the substrate surface in the one-stage encapsulating process. This is also evidenced by the good agreement between experiment and FEA results (Figure 1d,e). Figures S1–S3 (Supporting Information) provide additional FEA results and optical images of the serpentine interconnects at different view angles, which illustrated the detailed 3D configurations at different states of two-stage encapsulation. Due to the interaction with the deformed serpentine interconnects, the encapsulation layer also experiences nonuniform out-of-plane deformations (Figure S4, Supporting Information).

3. 2D Serpentine Interconnects

Quantitative mechanics modeling can serve as an important tool to optimize the processing parameters in the two-stage encapsulation process for 2D serpentine interconnects. The use of conventional one-stage encapsulations strategies and/or fully bonded 2D interconnects strongly limits the elastic stretchability, to values that are typically in the range of 10% or less. The two-stage encapsulation strategy can improve the elastic stretchability dramatically (e.g., more than six times) by adopting a proper

© 2019 WILEY-VCH Verlag GmbH & Co. KGaA, Weinheim

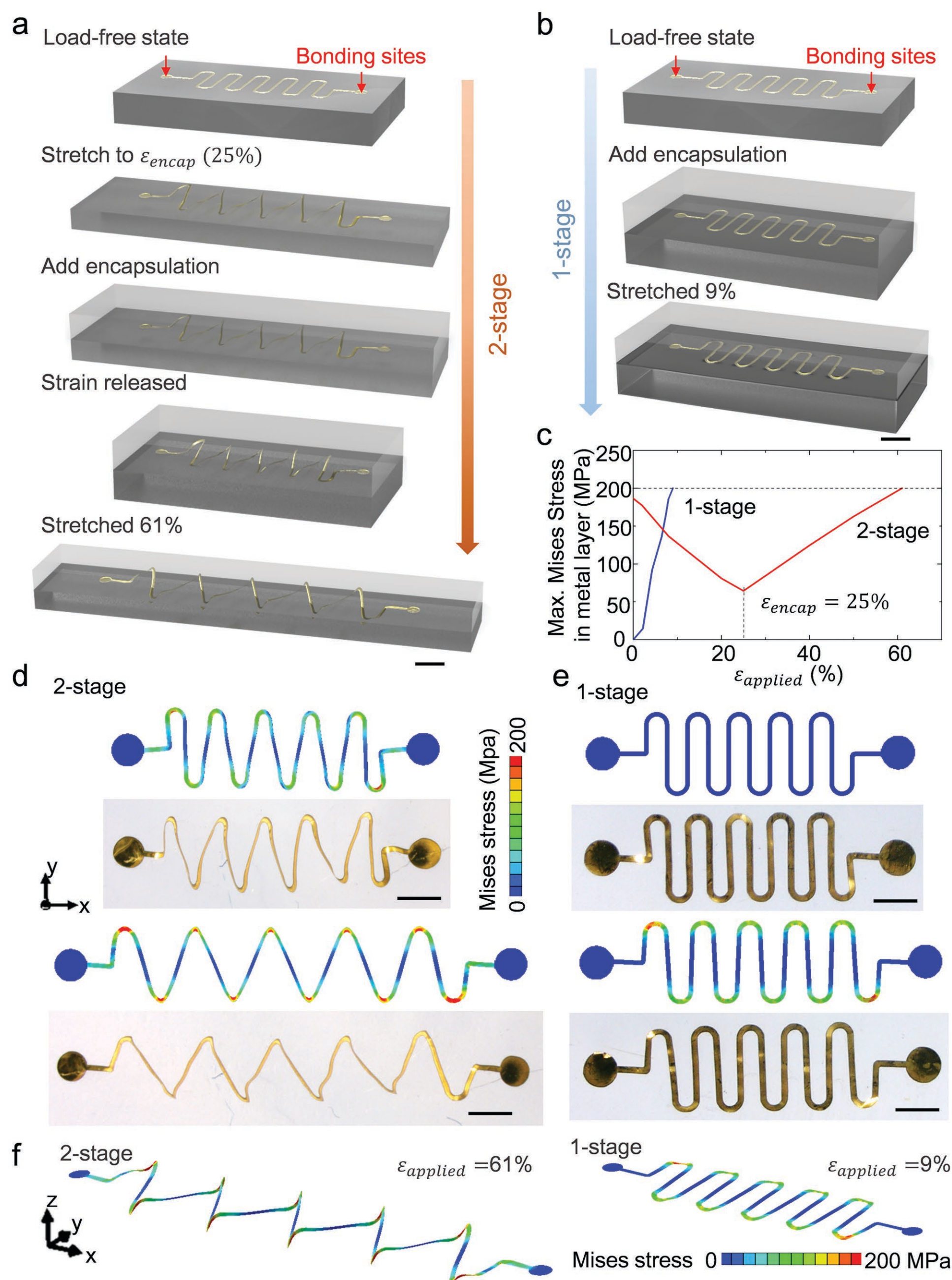

Figure 1. Schematic illustration of the proposed two-stage encapsulation strategy and conventional one-stage encapsulation strategy for 2D serpentine interconnects. a,b) Process of the a) two-stage and b) one-stage soft encapsulation strategy for 2D serpentine interconnects. For two-stage encapsulation strategy, the soft elastomer encapsulation is added while the substrate, on which the 2D serpentine interconnects are selectively bonded, is stretched to an encapsulating strain (ε_{encap}). Meanwhile for one-stage encapsulation strategy, the encapsulant is added at load-free state. c) Maximum Mises stress in the metal layer of the 2D serpentine interconnect as a function of the applied strain ($\varepsilon_{applied}$). d,e) FEA results and optical images on the undeformed and deformed configurations of a 2D serpentine interconnect with Mises stress distributions in the conditions of d) two-stage encapsulating processes (left, ε_{encap} = 26%) (top, load-free state; bottom, $\varepsilon_{applied}$ = 61%) and e) one-stage encapsulating process (right) (top, load-free state; bottom, $\varepsilon_{applied}$ = 9.0%). The key geometric parameters include t_{metal} = 0.4 µm, t_{PI} = 3.0 µm, width (w = 100 µm), amplitude (1.8 mm), and spacing (1.35 mm). The applied strain corresponds to the elastic stretchability. f) Similar results for the 2D serpentine interconnect in a perspective view. Scale bars, 1 mm.

encapsulating strain, as compared to the one-stage encapsulation (**Figure 2**a). The improvement in stretchability increases with increasing ε_{encap} up to a threshold ($\varepsilon_{encap-th}$, 25% and 26% for amplitude/spacing ratio = 3.33 and 4.00, respectively), beyond which plastic yielding occurs in the metal layer after full release of the prestretch. The threshold encapsulating strain ($\varepsilon_{encap-th}$) can be regarded as an optimal value to maximize the elastic stretchability during the two-stage

© 2019 WILEY-VCH Verlag GmbH & Co. KGaA, Weinheim

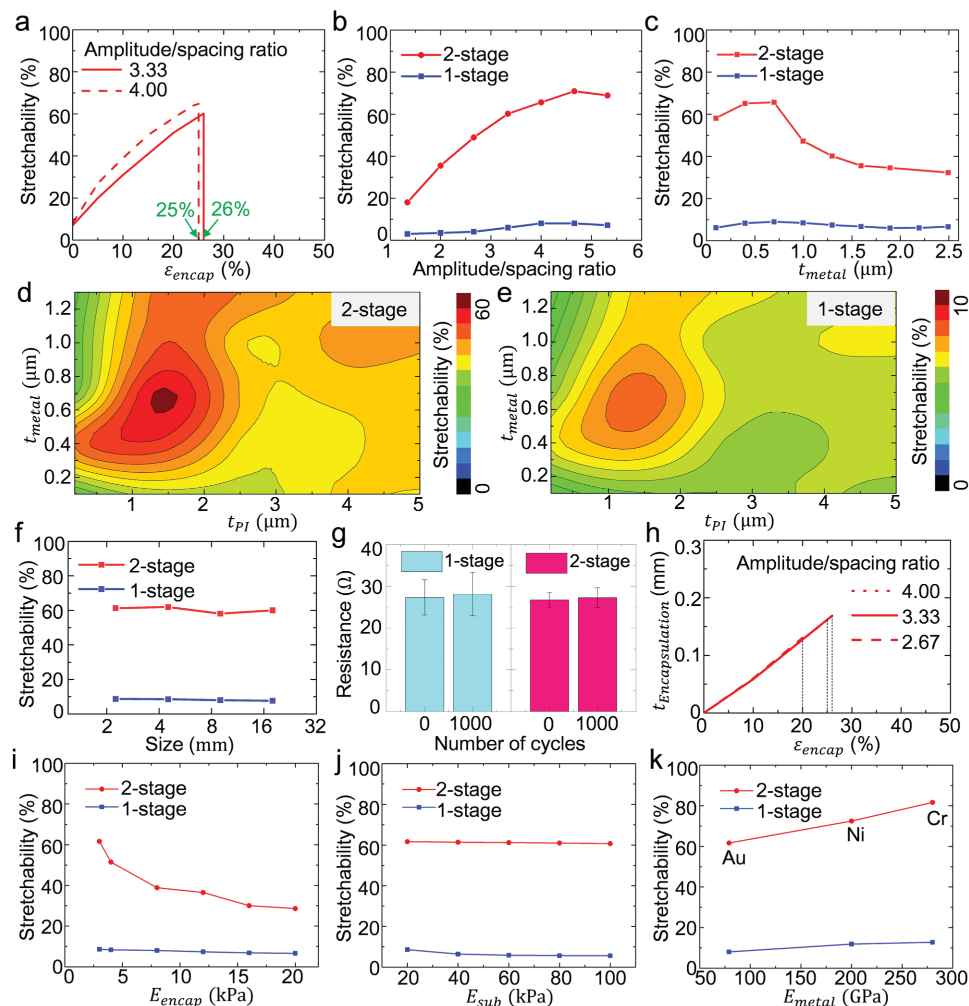

Figure 2. Mechanics of the two-stage encapsulation strategy for 2D serpentine interconnects. a) Elastic stretchability of an encapsulated 2D serpentine interconnect with use of different levels of encapsulating strains in the two-stage encapsulation strategy. b) Elastic stretchability of 2D serpentine interconnects formed with different amplitude/spacing ratios and c) different metal thicknesses, in both the conditions of one-stage and two-stage encapsulation. d,e) Contour plot of elastic stretchability in terms of metal thicknesses and PI thicknesses for 2D serpentine interconnects in the conditions of d) two-stage encapsulation and e) one-stage encapsulation. f) Scale effect on the elastic stretchability of 2D serpentine interconnects, where the size refers to the distance between the left-most and right-most bonding sites. g) Resistance of a 2D serpentine interconnect before and after cyclic stretching test. h) Encapsulation thickness of 2D serpentine interconnects in the two-stage process versus the encapsulating strain. Elastic stretchability of 2D serpentine interconnects using different i) encapsulation materials, j) substrate materials, and k) metal materials.

encapsulation. The amplitude/spacing ratio of the 2D serpentine interconnects represents a key design parameter that affects the elastic stretchability (Figure S5, Supporting Information). As compared to the one-stage encapsulation, in which the elastic stretchability changes relative slightly, the elastic stretchability in the two-stage encapsulation condition increases significantly with increasing the amplitude/spacing ratio (Figure 2b). The threshold encapsulating strains ($\varepsilon_{encap-th}$) for different amplitude/spacing ratios are in Figure S6 (Supporting Information). The metal thickness plays a crucial role in the resulting elastic stretchability of 2D serpentine interconnects, as evidenced by the FEA results in Figure 2c. To take full advantage of the sandwich (PI/metal/PI) design, the thicknesses of the metal layer and PI layer are changed simultaneously to study the variation of the elastic stretchability. The contour plots of elastic stretchability for the two-stage (Figure 2d) and one-stage (Figure 2e) encapsulating conditions both suggest an optimum set of thicknesses as $t_{PI}^{optimum} = 1.4$ μm and $t_{metal}^{optimum} = 0.4$ μm. In this set of calculations, some key geometric parameters of 2D serpentine interconnects include the width (w = 50 μm), amplitude (0.9 mm), and spacing (0.675 mm).

The two-stage encapsulation strategy is scalable across a large range of dimensions. As shown in Figure 2f, when the in-plane sizes are increased from 2.4 to 19.2 mm for fixed thicknesses of PI and metal layers, no obvious change in the elastic stretchability can be observed. Fatigue tests (Figure 2g and Figure S7, Supporting Information) demonstrate the robustness of the electrical interconnects. In particular, the resistances of the 2D serpentine interconnects change very slightly, after repetitively stretching the structures to 9% and 61% for one-stage and two-stage encapsulating conditions,

© 2019 WILEY-VCH Verlag GmbH & Co. KGaA, Weinheim

respectively, at a strain rate of 111% min^{-1} for a thousand cycles.

It is noteworthy that the thickness of the encapsulation can be very thin (<0.2 mm) for 2D serpentine interconnects with two-stage encapsulating strategy. When alternative encapsulating materials, substrate materials, and metal materials (e.g., Au, Ni, and Cr) are adopted, both the optimal encapsulating strain and the elastic stretchability vary, as shown in Figure 2i–k. For the two-stage encapsulation of 2D serpentine interconnects, the elastic stretchability depends highly on the encapsulation modulus, rather than the substrate modulus, because the buckled architectures mainly interface with the encapsulation material. Unlike the case for one-stage encapsulation, the elastic stretchability is more sensitive to the substrate modulus in the range considered herein. This sensitivity can be attributed to the planar configuration of the interconnects and their tight attachment to the substrate and the encapsulation materials and the fact that the substrate is more rigid than the encapsulant for these studies (Figure 2i,j). Figure 2k shows that the two-stage encapsulation strategy can improve the elastic stretchability substantially for other choices of metals as well. Effects of the encapsulation modulus, substrate modulus, and metal modulus on the threshold encapsulating strain of 2D serpentine interconnects are presented in Figure S8 (Supporting Information). In all of the cases considered herein, the two-stage encapsulation strategy can always enable an obvious improvement of the stretchability.

4. 2D Fractal-Inspired Interconnects and 3D Helical Interconnects

Existing studies demonstrated that free-standing interconnects with fractal-inspired 2D patterns can offer a larger elastic stretchability than 2D serpentine patterns, for a prescribed areal coverage of functional components in island-bridge designs.[65,76] Similar to 2D serpentine interconnects, the conventional one-stage solid encapsulation reduces the elastic stretchability of the 2D fractal interconnects to a relatively low level (e.g., ≈11%). By implementing the two-stage encapsulation strategy, the elastic stretchability can be increased by more than four times (i.e., to 46%), in comparison to the one-stage encapsulation, through a mechanism (i.e., formation of buckled 3D configurations during the prestretch) similar to that of the 2D serpentine interconnects. **Figure 3**a presents the FEA results of deformed configurations with Mises stress distribution, when the 2D fractal interconnect is stretched to the elastic limit, for both one-stage and two-stage encapsulation. Optical images collected at the same applied strains show good agreement with FEA. The fatigue tests shown in Figure 3b demonstrate the robustness and validate the FEA prediction of elastic stretchability in a quantitative manner. In particular, the cyclic test of uniaxial stretching with a fixed strain rate of 67% min^{-1} was performed for the 2D fractal-inspired interconnects under both the one-stage and two-stage encapsulation. The resistance was measured after every 100 cycles. The experimental results showed that the 2D fractal-inspired interconnect under one-stage encapsulation process survives 1000 cycles for the strain amplitude of 11%, as evidenced by the negligible resistance change. But the interconnect fails after 900 and 700 cycles, for the strain amplitudes of 13% and 15%, respectively. Optical images in Figure 3c present the cracked sections in the interconnects, which coincide with the locations of strain concentration predicted by FEA (Figure 3a). These experimental results suggest the elastic stretchability to be in the range of 11%–13%, which is in accordance with the FEA result (≈11%). In the condition of two-stage encapsulation, the experimental results also show good agreement with FEA predictions, as presented in Figure 3b,c (bottom).

The metal thickness of the 2D fractal-inspired interconnects also plays a significant role in the elastic stretchability. A representative set of FEA results appears in Figure 3d, where the elastic stretchability of 2D fractal-inspired interconnects with the two-stage encapsulation strategy decreases with increasing the metal thickness. By contrast, with the change of metal thickness, the 2D fractal-inspired interconnects under the one-stage encapsulation exhibit three types of deformation modes, namely, wrinkling, buckling, and scissoring.[57] For the mode of wrinkling, a local maximum (≈10%) appears at $t_{metal} = 0.4$ µm. For the mode of buckling, the elastic stretchability increases slightly with increasing the thickness, due to the transition into the scissoring mode without any out-of-plane deformations. Despite these differences, the two-stage encapsulation strategy holds a substantial advantage of the resulting elastic stretchability over the one-stage process, for a very wide range of metal thicknesses. Further optimization of elastic stretchability for different metal thicknesses and PI thicknesses is presented in Figure S9 (Supporting Information).

It is also noteworthy that with the two-stage encapsulating strategy, the minimum thickness of the encapsulation layer to fully cover the buckled interconnects is typically below 0.3 mm (Figure 3e), which does not affect the flexibility of the entire structure significantly. The elastic stretchability of 2D fractal-inspired interconnects with two-stage encapsulation process also depends highly on the encapsulation modulus rather than the substrate modulus. This follows from a similar mechanism to the 2D serpentine interconnects that the buckled configurations mainly interact with the encapsulation material (Figure 3f,g). When alternative metal materials with a higher modulus are adopted for the interconnects, the elastic stretchability can be improved slightly (Figure 3h). Similar trends of the encapsulating strain are shown in Figure S10 (Supporting Information).

The two-stage encapsulation strategy can also be extended to the 3D helical configurations formed via mechanically guided assembly techniques, as reported in recent years.[67,80,82,83] Compared with the 2D serpentine interconnects, 3D helical interconnects showed higher mechanical compliance because of their smooth and low strain distribution reacting to stretching load, as demonstrated by Jang et al.[67] Despite this advance, the stretchability of 3D helical interconnects is severely limited even ultrasoft elastomer (E = 3 kPa; Silbione 4717A/B, Bluestar Silicones, France) is employed as encapsulation material (Figure S11, Supporting Information). Applying the two-stage encapsulating process can increase the elastic stretchability by a factor of ≈2.6, in comparison to the one-stage process (Figures S12 and S14, Supporting Information). Here, the key

© 2019 WILEY-VCH Verlag GmbH & Co. KGaA, Weinheim

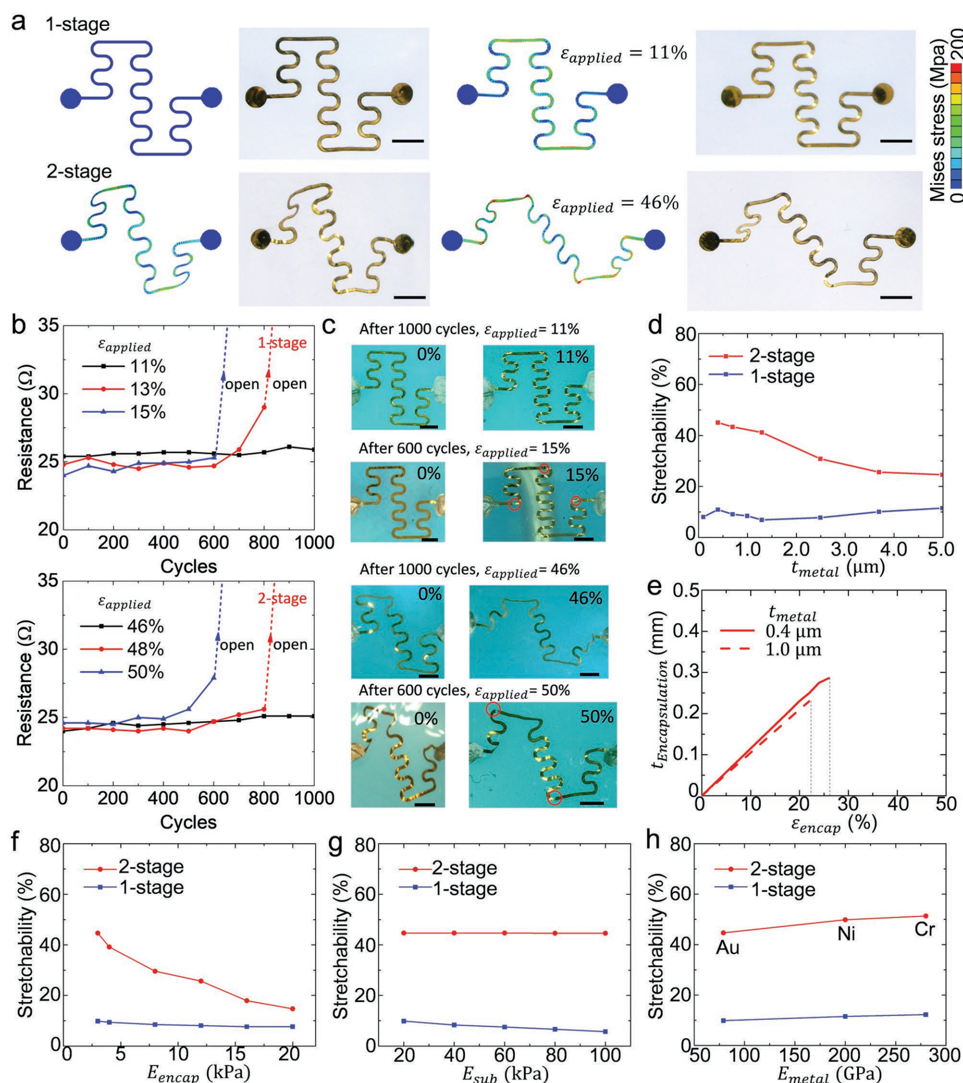

Figure 3. Mechanics of the two-stage encapsulation strategy for 2D fractal-inspired interconnects. a) Optical images and FEA results on the undeformed and deformed configurations of a 2D fractal interconnect with Mises stress distributions in the conditions of one-stage and two-stage encapsulating processes (ε_{encap} = 22%). The left figures present the load-free state, and the right figures present the deformed state stretched to the elastic limit. Scale bars, 1 mm. b) Variation of the resistance for the 2D fractal-inspired interconnects with one-stage (top) and two-stage (bottom) encapsulating processes under different levels of strain amplitudes. c) Optical images of the interconnects (with one-stage encapsulation) after 1000 cycles with a strain amplitude of 11% and 600 cycles with a strain amplitude of 15%, and similar results (with two-stage encapsulation) after 1000 cycles with a strain amplitude of 46% and 600 cycles with a strain amplitude of 50%. Here, the red circles highlight the cracked sections. Scale bars, 1 mm. d) Elastic stretchability of 2D fractal-inspired interconnects formed with different metal thicknesses, in both conditions of one-stage and two-stage encapsulation strategy. e) Encapsulation thickness of 2D fractal-inspired interconnects in the two-stage process versus the encapsulating strain. Elastic stretchability of 2D fractal-inspired interconnects using different f) encapsulation materials, g) substrate materials, and h) metal materials.

geometric parameters of the 2D precursor for the formation of 3D helical interconnects include the width (w = 50 μm), central arc angle (θ_0 = 180°), and arc radius (0.425 mm) (Figure S15, Supporting Information). For the 3D helical interconnects, the encapsulation effect on the elastic stretchability depends highly on the prestrain (ε_{pre}) and the geometric parameters of the 2D precursor adopted in the 3D assembly. Figure S16 (Supporting Information) shows that the elastic stretchability increases with increasing ε_{pre} at the initial stage in both conditions of one-stage and two-stage encapsulation, because the 3D helical interconnects become denser. Beyond a critical prestrain, the elastic stretchability decreases with the further increase of ε_{pre}. Such a nonmonotonous dependence results from distinct reasons for the one-stage and two-stage encapsulating processes. During the one-stage encapsulation, a knot-like structure forms when a sufficiently large ε_{pre} is adopted, which cannot be effectively unravelled during stretching, thereby limiting the further increase of elastic stretchability. During the two-stage encapsulation, the threshold encapsulating strain ($\varepsilon_{encap-th}$) dramatically decreases at a large ε_{pre} (Figure S17, Supporting Information), which results in a reduction in the elastic stretchability beyond $\varepsilon_{pre} \approx$ 200%. Despite these limits, the two-stage encapsulation strategy enables a significant improvement in the

© 2019 WILEY-VCH Verlag GmbH & Co. KGaA, Weinheim

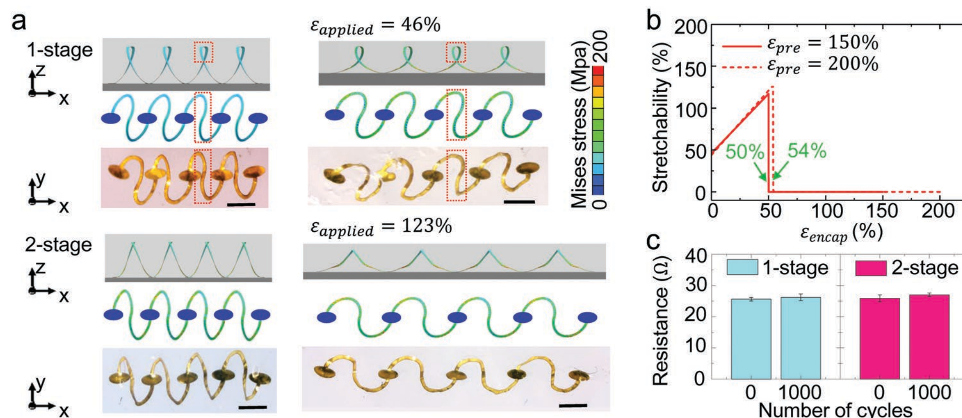

Figure 4. Mechanics of the two-stage encapsulation strategy for 3D helical interconnects. a) Optical images and FEA results on the undeformed and deformed configurations of a 3D helical interconnect with Mises stress distributions in the conditions of one-stage (top, $\varepsilon_{encap} = 0\%$) (left, load-free state; right, $\varepsilon_{applied} = 46\%$) and two-stage encapsulating processes (bottom, $\varepsilon_{encap} = 50\%$) (left, load-free state; right, $\varepsilon_{applied} = 123\%$) (scale bars, 1 mm). The key geometric parameters of the 2D precursor used in the 3D assembly include $\varepsilon_{pre} = 150\%$, $t_{metal} = 0.4$ µm, $t_{PI} = 3.0$ µm, width ($w = 100$ µm), central arc angle ($\theta_0 = 180°$), and arc radius (0.85 mm). b) Elastic stretchability of an encapsulated 3D helical interconnect with use of different levels of encapsulating strains in the two-stage encapsulation strategy. c) Resistance of a four-unit 3D helical interconnect presented in (a) before and after cyclic stretching test.

elastic stretchability over the one-stage strategy for all prestrains (up to approximately four times for ε_{pre}= 250%). Such knot-like structures formed in the conventional one-stage encapsulation mainly result from in-plane rotational motions at the peaks of the helices (**Figure 4**a) and become evident when using high levels of prestrain (ε_{pre}) in the 3D assembly. The two-stage encapsulation strategy avoids the formation of such knot-like structures by prestretching the substrate prior to adding the encapsulation. This mechanism is highlighted by the optical images of deformed configurations based on experiments (Figure 4a), which also agree reasonably well with FEA.

Figure 4b shows that the use of ε_{encap} above a certain threshold (50% and 54% for ε_{pre} = 150% and 200%, respectively) can lead to plastic yielding of the 3D helical interconnects before full release of the prestretch in the substrate. Below such a threshold, the elastic stretchability increases monotonically with increasing ε_{encap}, indicating an enhancement in stretchability by a factor of more than two for $\varepsilon_{encap} > 39\%$. Fatigue tests (Figure 4b) demonstrate the robustness of the electrical interconnects. The metal thickness also plays a crucial role, as evidenced by the FEA results in Figure S18 (Supporting Information). When the metal thickness is larger than a critical value, the elastic stretchability is totally suppressed, because plastic yielding occurs in the metal layer during the mechanically guided 3D assembly, and any further external loading induces irreversible deformations. Further optimization that considers both the PI thickness and metal thickness appears in Figure S19 (Supporting Information). The two-stage encapsulation strategy is also scalable across a large range of sizes for the 3D helical interconnects (Figure S20, Supporting Information). The thickness of encapsulation layer can also be very thin, typically below 0.6 mm for the cases studied herein (Figure S21, Supporting Information). The dependences of the elastic stretchability on the moduli of encapsulation material, substrate material, and metal material are presented in Figures S22 and S23 (Supporting Information), showing similar trends with the 2D serpentine interconnects.

5. Highly Stretchable LED Systems with Solid Encapsulation

The reported two-stage encapsulation strategy has general utility across a broad range of stretchable electronic devices. As an example, we demonstrated an encapsulated device in the form of highly stretchable LED systems that use networks of 2D fractal interconnects (**Figure 5**a,b). For the conventional one-stage encapsulation, the elastic stretchability of the device system is only ≈10% for uniaxial or biaxial stretching (Figure 5c). This elastic stretchability is significantly increased, by a factor of approximately four (to ≈40%), with use of the two-stage encapsulation strategy, as illustrated in Figure 5d. Experimental results (Figures S24 and S25, Supporting Information) under the cyclic biaxial stretching and relaxing with a fixed strain rate of 77% min^{-1} verify such a stretchability enhancement. In particular, the stretchable LED systems under one-stage encapsulation survive 1000 cycles for the strain amplitude of 9.6%, and fail after 400 cycles for the strain amplitude of 12%. The two-stage encapsulation enhances the elastic stretchability significantly to the range of 40%–42%, according to the cyclic test. The experimental results in Figure 5d present encapsulated working devices under such levels of stretching. Practical demonstrations with coupled bending and folding deformations show that the encapsulated device can be mounted onto complex curvilinear surfaces (Figure 5e), as an additional indication of excellent mechanical properties.

Another encapsulated device demonstration is a 3D electromagnetic (EM) energy harvester that can power commercial LEDs, as presented in **Figure 6**a,b. This system exploits a spring-like 3D helical architecture to serve both as the antenna and as the interconnects. The entire system was

 © 2019 WILEY-VCH Verlag GmbH & Co. KGaA, Weinheim

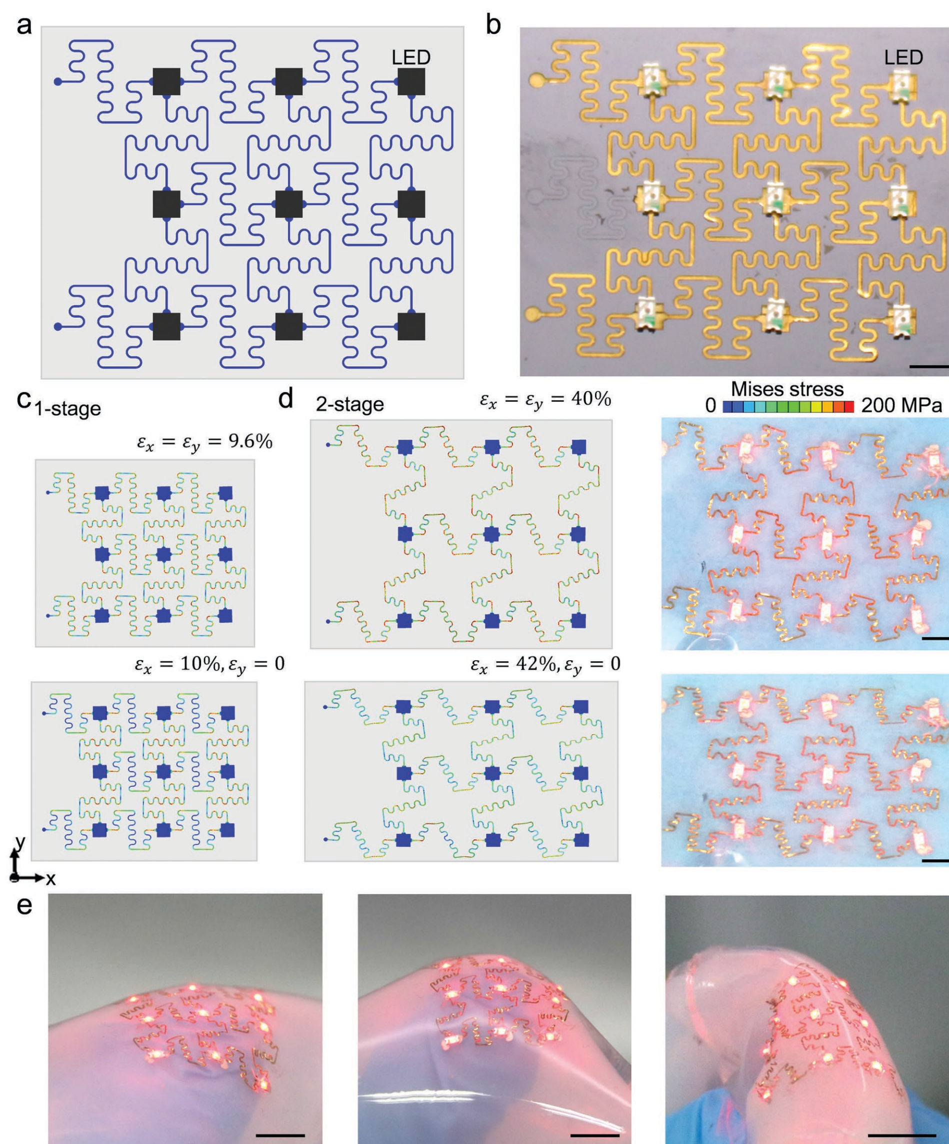

Figure 5. Highly stretchable LED systems with solid encapsulation. a) Illustration of the device with a 3 × 3 array consisting of 2D fractal interconnects. b) Optical image of an experimentally realized device (scale bar, 1 mm). c) System-level deformations under uniaxial and biaxial stretching and Mises stress distribution determined by FEA in the conditions of c) one-stage and d) two-stage encapsulating processes. Optical images are shown in (d) for the two-stage encapsulation (scale bars, 1 mm). e) Optical images of the working device under different forms of complex mechanical loadings. This device is formed using the two-stage encapsulation strategy with encapsulating strain ε_{encap} = 25% (scale bars, 5 mm).

formed through the mechanically guided 3D assembly, in which an equal biaxial prestrain of ε_{pre} = 150% was adopted (Figure S26, Supporting Information). With a solid encapsulation, the elastic stretchability of the 3D device system is smaller than that of the individual unit cell of the 3D coil, in part due to the complicated interactions between elastomer encapsulation and closely distributed 3D coils, as presented in Figure 6c. In comparison to the one-stage encapsulation, the elastic stretchabilities under both uniaxial and biaxial loadings are improved by a factor of around four, through use of the two-stage encapsulation with ε_{encap} = 30% (Figure 6d). With the two-stage encapsulation strategy, this device system offers ultrahigh elastic stretchabilities (102% and 94% for uniaxial and biaxial stretching, respectively). For such complex 3D constructions, the FEA can capture well the detailed deformations at different locations of the device, as evidenced by the agreement with the experimental results. We characterized the EM property of the antenna by experimental measurement and EM simulations using the commercial software HFSS as presented in Figure 6e. The difference of return loss parameter (S11) between the load-free state and stretched (50%) state is relatively small, as shown by both the simulation and experiment results. Optical images of the working device presented in Figure 6f prove the functionality under a large uniaxial stretch.

© 2019 WILEY-VCH Verlag GmbH & Co. KGaA, Weinheim

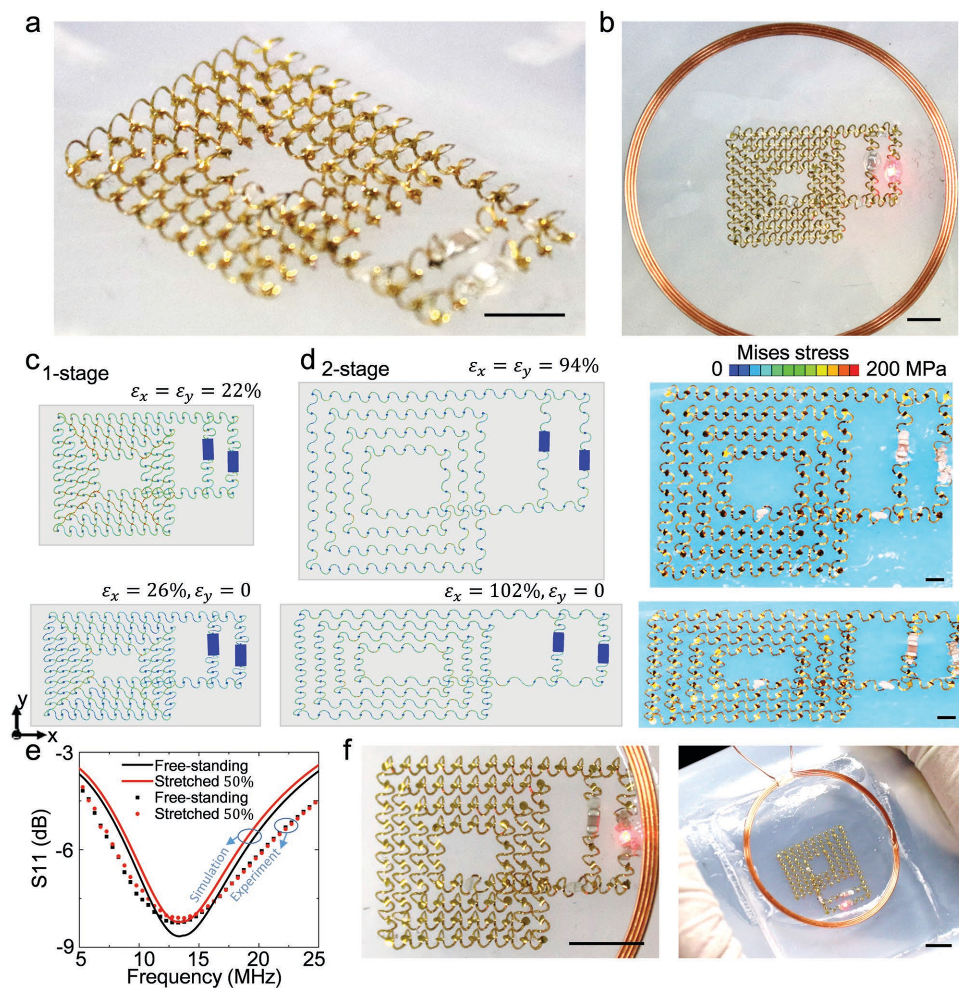

Figure 6. 3D soft antenna system with solid encapsulation. a,b) Optical images of a fabricated 3D soft antenna consisting of helical mesostructures, with a) a perspective view and b) a top view. c) System-level deformations under uniaxial and biaxial stretching and Mises stress distribution determined by FEA in the conditions of c) one-stage and d) two-stage encapsulating processes. Optical images are shown in (d) for the two-stage encapsulation (scale bars, 1 mm). e) Electromagnetic (EM) characterization of the 3D helical antenna, showing the return loss parameter (S11) versus frequency based on EM simulation and experiment measurements. f) Optical images of the working device, in the undeformed and uniaxially stretched (50%) states, respectively (scale bars, 5 mm).

6. Conclusion

In summary, we developed a generic solid encapsulation method, capable of offering unprecedented elastic stretchabilities for a broad range of interconnect configurations. In comparison to the conventional one-stage encapsulation, the proposed two-stage encapsulation can enable an increase of stretchability by factors of approximately six for 2D serpentine interconnects, approximately four for 2D fractal interconnects, and ≈2.6 for 3D helical interconnects. Combined theoretical and experimental studies elucidated the underlying mechanisms of such stretchability enhancement and the effects of various design parameters. Device demonstrations in encapsulated soft LED systems constructed with 3D helical interconnects and 2D fractal interconnects show the ultrahigh stretchability can be well maintained at the device level. The presented soft encapsulation strategy has general utility in various stretchable interconnect technologies, and therefore has promising applications in the design of stretchable devices with different targeted applications.

7. Experimental Section

Experiment—Fabrication of the Encapsulated 3D Helical Interconnects: Spin-casting poly(methyl methacrylate) (PMMA; ≈100 nm in thickness, Microchem, USA) formed a thin sacrificial layer on a silicon wafer. Spin-casting PI (≈3 µm in thickness, Sigma-Aldrich, USA), depositing thin layers of metal by electron beam evaporation (Cr/Au, thickness 10/400 nm), and spin-casting another layer of polyimide followed by femtosecond laser cutting (Rofin, Deutsch) defined a network of 2D serpentine structures, here referred to as the 2D precursor. Dissolving the PMMA by immersion in acetone for 10 min allowed retrieval of the 2D precursor onto the surface of a polydimethylsiloxane (PDMS) stamp (Sylgard 184, Dow Corning Corporation, USA). Selective gumming of silicone rubber (705, RTV, NanDa, China) through a shadow mask (i.e., a thin (0.1 mm) sheet of polyethylene terephthalate (PET) film patterned with laser cutting) defined sites for strong bonding to a

© 2019 WILEY-VCH Verlag GmbH & Co. KGaA, Weinheim

silicone elastomer substrate (thickness 1 mm; Ecoflex 00-30A/B, Smooth-on, USA). A custom mechanical stage allowed application of precisely controlled levels of biaxial strain to this elastomer. Transfer printing the 2D precursor onto a prestrained substrate and stewing (12 h, 23 °C) the system activated the formation of strong bonds between the patterned 2D precursor and the surface of the silicone substrate. Partially releasing this prestrain (two-stage encapsulation) or fully releasing this prestrain (one-stage encapsulation) followed by casting a uniform layer of an ultralow-modulus elastomer (Silbione 4717A/B, Bluestar Silicones, France) encapsulated the entire system while preserving freedom of motion of the helical coils upon application of strain.

Experiment—Fabrication of the Encapsulated 2D Serpentine and 2D Fractal Inspired Interconnects: Most of the processes are similar to those described in the previous section. In the preparation of 2D serpentine (and 2D fractal-inspired) structures, transfer printing the 2D precursor onto a load-free substrate formed the interconnects for encapsulation. Prestretching the substrate (two-stage encapsulation) or keeping the zero strain state (one-stage encapsulation) followed by casting a uniform layer of an ultralow-modulus elastomer (Silbione 4717A/B) completed the encapsulation.

Experiment—Circuit Design and Test of the Soft LED System: In the circuit consisting of 3D helical coils, resonant inductive coupling using a network of unshielded 3D helical coil served as the basis for a wireless power receiver. A parallel capacitor (180 pF) defined a resonance at 13.56 MHz, as measured using an RF Impedance Analyzer (4291A, Hewlett Packard). The transmitter consisted of a circular wire wound coil with a radius of 43 mm, matched at 13.56 MHz, powered with an amplifier module (WSPAS-11000, Wattsine, China). With this system, the circuit is capable of operating the system to light the LED. In the circuit constructed with an array of 2D fractal interconnects, the DC power (15 V, 610E, TREK, USA) supply is directly exploited.

Experiment—Cyclic Stretching Test of the 3D Helical and 2D Serpentine Interconnects: A customized biaxial mechanical stretcher allowed precise control of strain applied to the substrate. A low strain rate (1000 cycles, 50 mm min^{-1}) was used in the cyclic stretching tests. Four sets of experiments were performed for the 3D helical interconnects and 2D serpentine interconnects formed with the one-stage and two-stage encapsulating processes, respectively. The resistances in these interconnects were measured before and after the cyclic stretching test.

Finite Element Analysis: 3D finite element analysis allowed prediction of the mechanical deformations and the Mises stress distributions of the individual 2D serpentine, 2D fractal interconnects, and 3D coils, as well as the network designs. Four-node shell elements with a three-layer (PI/metal/PI) composite modeled the 2D and 3D interconnects, and eight-node solid elements modeled the encapsulation and substrate. Refined meshes ensured the computational accuracy using commercial software (ABAQUS). To evaluate the stretchability in the encapsulated condition, the 3D and 2D interconnects are embedded in the encapsulation material and tied onto the substrate by predefined constraints. The elastic stretchability corresponds to the point at which the metal layer exceeds the yield strength (≈200 MPa for Au) across one quarter of the width of any section of the interconnect, and this criterion is supported by previous experimental studies.[76,84] A hyperelastic constitutive relation, i.e., the Mooney–Rivlin law, captured the properties of the elastomeric encapsulation ($E_{\text{encapsulation}}$ = 3 kPa and $\nu_{\text{encapsulation}}$ = 0.49) and substrate material ($E_{\text{substrate}}$ = 20 kPa and $\nu_{\text{substrate}}$ = 0.49). The relevant material parameters are (C_{10} = 0.40 kPa, C_{01} = 0.10 kPa, D_1 = 0.04 kPa^{-1}) for the encapsulation and (C_{10} = 2.68 kPa, C_{01} = 0.67 kPa, D_1 = 0.006 kPa^{-1}) for the substrate in ABAQUS. The other material parameters used are: E_{PI} = 2.5 GPa, ν_{PI} = 0.27 for polyimide; and E_{Au} = 79 GPa, ν_{Au} = 0.27 for gold. Here, E is elastic modulus and ν is Poisson's ratio.

Electromagnetic Simulation: The finite element method was used in the electromagnetic simulations to get the return loss parameter (S11) of the 3D soft antenna. The simulations were performed using the commercial software Ansys HFSS (Ansys HFSS 13 User's guide, Ansys Inc. 2011), where the lumped port was used, and the port impedance was set according to the matched capacitor (180 pF). The adaptive mesh (tetrahedron elements) together with a spherical surface (2000 mm in radius) as the radiation boundary was adopted to ensure computational accuracy. The material parameters include the relative permittivity (ε_r), relative permeability (μ_r), and conductivity (σ) of Au, PI, Ecoflex, and Silbione, i.e., ε_r(Au) = 1, μ_r(Au) = 0.99996, and σ(Au) = 4.1 × 10^7 S/m; ε_r(PI) = 3.5, μ_r(PI) = 1, and σ_{PI} = 0 S/m; ε_r(Ecoflex) = 2.8, μ_r(Ecoflex) = 1, and σ(Ecoflex) = 0 S/m; and ε_r(Silbione) = 4.4, μ_r(Silbione) = 1, and σ(Silbione) = 0 S/m.

Supporting Information

Supporting Information is available from the Wiley Online Library or from the author.

Acknowledgements

K.L. and X.C. contributed equally to this work. Y.Z. acknowledges the support from the National Natural Science Foundation of China (Grant Nos. 11502129 and 11722217) and the Tsinghua National Laboratory for Information Science and Technology. X.F. acknowledges support from the National Natural Science Foundation of China (Grant No. 11320101001) and the National Basic Research Program of China (Grant No. 2015CB351900). Z.X. acknowledges the support from the National Natural Science Foundation of China (Grant No. 11402134). Y.H. acknowledges the support from NSF (Grant Nos. 1400169, 1534120, and 1635443).

Conflict of Interest

The authors declare no conflict of interest.

Keywords

buckling, encapsulation method, soft elastomers, stretchable electronics, two-stage encapsulation

Received: September 19, 2018
Revised: December 2, 2018
Published online: January 9, 2019

[1] M. Kaltenbrunner, T. Sekitani, J. Reeder, T. Yokota, K. Kuribara, T. Tokuhara, M. Drack, R. Schwödiauer, I. Graz, S. Bauer-Gogonea, *Nature* **2013**, *499*, 458.
[2] C. Keplinger, J.-Y. Sun, C. C. Foo, P. Rothemund, G. M. Whitesides, Z. Suo, *Science* **2013**, *341*, 984.
[3] D.-Y. Khang, H. Jiang, Y. Huang, J. A. Rogers, *Science* **2006**, *311*, 208.
[4] D.-H. Kim, N. Lu, R. Ma, Y.-S. Kim, R.-H. Kim, S. Wang, J. Wu, S. M. Won, H. Tao, A. Islam, *Science* **2011**, *333*, 838.
[5] S. Lee, A. Reuveny, J. Reeder, S. Lee, H. Jin, Q. Liu, T. Yokota, T. Sekitani, T. Isoyama, Y. Abe, *Nat. Nanotechnol.* **2016**, *11*, 472.
[6] I. R. Minev, P. Musienko, A. Hirsch, Q. Barraud, N. Wenger, E. M. Moraud, J. Gandar, M. Capogrosso, T. Milekovic, L. Asboth, *Science* **2015**, *347*, 159.
[7] J. Y. Oh, S. Rondeau-Gagné, Y.-C. Chiu, A. Chortos, F. Lissel, G.-J. N. Wang, B. C. Schroeder, T. Kurosawa, J. Lopez, T. Katsumata, *Nature* **2016**, *539*, 411.

© 2019 WILEY-VCH Verlag GmbH & Co. KGaA, Weinheim

[8] H. Ota, K. Chen, Y. Lin, D. Kiriya, H. Shiraki, Z. Yu, T.-J. Ha, A. Javey, *Nat. Commun.* **2014**, *5*, 5032.
[9] T. Sekitani, H. Nakajima, H. Maeda, T. Fukushima, T. Aida, K. Hata, T. Someya, *Nat. Mater.* **2009**, *8*, 494.
[10] T. Sekitani, Y. Noguchi, K. Hata, T. Fukushima, T. Aida, T. Someya, *Science* **2008**, *321*, 1468.
[11] D. Son, J. Lee, S. Qiao, R. Ghaffari, J. Kim, J. E. Lee, C. Song, S. J. Kim, D. J. Lee, S. W. Jun, *Nat. Nanotechnol.* **2014**, *9*, 397.
[12] Z. Song, T. Ma, R. Tang, Q. Cheng, X. Wang, D. Krishnaraju, R. Panat, C. K. Chan, H. Yu, H. Jiang, *Nat. Commun.* **2014**, *5*, 3140.
[13] Z. Song, X. Wang, C. Lv, Y. An, M. Liang, T. Ma, D. He, Y.-J. Zheng, S.-Q. Huang, H. Yu, *Sci. Rep.* **2015**, *5*, 10988.
[14] J. Y. Sun, C. Keplinger, G. M. Whitesides, Z. Suo, *Adv. Mater.* **2014**, *26*, 7608.
[15] C. Wang, D. Hwang, Z. Yu, K. Takei, J. Park, T. Chen, B. Ma, A. Javey, *Nat. Mater.* **2013**, *12*, 899.
[16] F. Xu, W. Lu, Y. Zhu, *ACS Nano* **2011**, *5*, 672.
[17] J. Xu, S. Wang, G.-J. N. Wang, C. Zhu, S. Luo, L. Jin, X. Gu, S. Chen, V. R. Feig, J. W. To, *Science* **2017**, *355*, 59.
[18] Y. Zhu, F. Xu, *Adv. Mater.* **2012**, *24*, 1073.
[19] X. Huang, Y. Liu, H. Cheng, W. J. Shin, J. A. Fan, Z. Liu, C. J. Lu, G. W. Kong, K. Chen, D. Patnaik, *Adv. Funct. Mater.* **2014**, *24*, 3846.
[20] Y. Li, J. Zhang, Y. Xing, J. Song, *J. Appl. Mech.* **2017**, *84*, 111004.
[21] J. Song, X. Feng, Y. Huang, *Natl. Sci. Rev.* **2016**, *3*, 128.
[22] J. Bian, Y. Ding, Y. Duan, X. Wan, Y. Huang, *Soft Matter* **2017**, *13*, 7244.
[23] Y. Cui, Y. Li, Y. Xing, *Int. J. Heat Mass Transfer* **2018**, *127*, 97.
[24] K. Zhang, Y. H. Jung, S. Mikael, J.-H. Seo, M. Kim, H. Mi, H. Zhou, Z. Xia, W. Zhou, S. Gong, *Nat. Commun.* **2017**, *8*, 1782.
[25] S. P. Lacour, G. Courtine, J. Guck, *Nat. Rev. Mater.* **2016**, *1*, 16063.
[26] J. A. Rogers, *JAMA, J. Am. Med. Assoc.* **2015**, *313*, 561.
[27] J. A. Rogers, T. Someya, Y. Huang, *Science* **2010**, *327*, 1603.
[28] T. Someya, Z. Bao, G. G. Malliaras, *Nature* **2016**, *540*, 379.
[29] Y. Huang, Y. Ding, J. Bian, Y. Su, J. Zhou, Y. Duan, Z. Yin, *Nano Energy* **2017**, *40*, 432.
[30] Y. Ma, M. Pharr, L. Wang, J. Kim, Y. Liu, Y. Xue, R. Ning, X. Wang, H. U. Chung, X. Feng, *Small* **2017**, *13*, 1602954.
[31] S. Kabiri Ameri, R. Ho, H. Jang, L. Tao, Y. Wang, L. Wang, D. M. Schnyer, D. Akinwande, N. Lu, *ACS Nano* **2017**, *11*, 7634.
[32] W. Gao, S. Emaminejad, H. Y. Y. Nyein, S. Challa, K. Chen, A. Peck, H. M. Fahad, H. Ota, H. Shiraki, D. Kiriya, *Nature* **2016**, *529*, 509.
[33] M. Bariya, H. Y. Y. Nyein, A. Javey, *Nat. Electron.* **2018**, *1*, 160.
[34] S. Emaminejad, W. Gao, E. Wu, Z. A. Davies, H. Y. Y. Nyein, S. Challa, S. P. Ryan, H. M. Fahad, K. Chen, Z. Shahpar, *Proc. Natl. Acad. Sci. USA* **2017**, *114*, 4625.
[35] E. T. Filipov, T. Tachi, G. H. Paulino, *Proc. Natl. Acad. Sci. USA* **2015**, *112*, 12321.
[36] C. Choi, M. K. Choi, S. Liu, M. S. Kim, O. K. Park, C. Im, J. Kim, X. Qin, G. J. Lee, K. W. Cho, *Nat. Commun.* **2017**, *8*, 1664.
[37] Y. H. Jung, T.-H. Chang, H. Zhang, C. Yao, Q. Zheng, V. W. Yang, H. Mi, M. Kim, S. J. Cho, D.-W. Park, *Nat. Commun.* **2015**, *6*, 7170.
[38] D. J. Lipomi, M. Vosgueritchian, B. C. Tee, S. L. Hellstrom, J. A. Lee, C. H. Fox, Z. Bao, *Nat. Nanotechnol.* **2011**, *6*, 788.
[39] D.-W. Park, J. P. Ness, S. K. Brodnick, C. Esquibel, J. Novello, F. Atry, D.-H. Baek, H. Kim, J. Bong, K. I. Swanson, *ACS Nano* **2018**, *12*, 148.
[40] J. H. Seo, K. Zhang, M. Kim, D. Zhao, H. Yang, W. Zhou, Z. Ma, *Adv. Opt. Mater.* **2016**, *4*, 120.
[41] L. Song, A. C. Myers, J. J. Adams, Y. Zhu, *ACS Appl. Mater. Interfaces* **2014**, *6*, 4248.
[42] G. J. N. Wang, A. Gasperini, Z. Bao, *Adv. Electron. Mater.* **2018**, *4*, 1700429.
[43] T. Wang, H. Yang, D. Qi, Z. Liu, P. Cai, H. Zhang, X. Chen, *Small* **2018**, *14*, 1702933.
[44] S. Yao, Y. Zhu, *Nanoscale* **2014**, *6*, 2345.
[45] C. Yu, X. Li, T. Ma, J. Rong, R. Zhang, J. Shaffer, Y. An, Q. Liu, B. Wei, H. Jiang, *Adv. Energy Mater.* **2012**, *2*, 68.
[46] C. Yu, C. Masarapu, J. Rong, B. Wei, H. Jiang, *Adv. Mater.* **2009**, *21*, 4793.
[47] H. Jiang, D.-Y. Khang, J. Song, Y. Sun, Y. Huang, J. A. Rogers, *Proc. Natl. Acad. Sci. USA* **2007**, *104*, 15607.
[48] Y. Sun, W. M. Choi, H. Jiang, Y. Y. Huang, J. A. Rogers, *Nat. Nanotechnol.* **2006**, *1*, 201.
[49] T. Pan, M. Pharr, Y. Ma, R. Ning, Z. Yan, R. Xu, X. Feng, Y. Huang, J. A. Rogers, *Adv. Funct. Mater.* **2017**, *27*, 1702589.
[50] S. Yang, Y. C. Chen, L. Nicolini, P. Pasupathy, J. Sacks, B. Su, R. Yang, D. Sanchez, Y. F. Chang, P. Wang, *Adv. Mater.* **2015**, *27*, 6423.
[51] K. Liu, J. Wu, G. H. Paulino, H. J. Qi, *Sci. Rep.* **2017**, *7*, 3511.
[52] Y. Gao, Y. Zhang, X. Wang, K. Sim, J. Liu, J. Chen, X. Feng, H. Xu, C. Yu, *Sci. Adv.* **2017**, *3*, e1701222.
[53] C. Wang, K. Sim, J. Chen, H. Kim, Z. Rao, Y. Li, W. Chen, J. Song, R. Verduzco, C. Yu, *Adv. Mater.* **2018**, *30*, 1706695.
[54] J. Viventi, D.-H. Kim, L. Vigeland, E. S. Frechette, J. A. Blanco, Y.-S. Kim, A. E. Avrin, V. R. Tiruvadi, S.-W. Hwang, A. C. Vanleer, *Nat. Neurosci.* **2011**, *14*, 1599.
[55] H. Jinno, K. Fukuda, X. Xu, S. Park, Y. Suzuki, M. Koizumi, T. Yokota, I. Osaka, K. Takimiya, T. Someya, *Nat. Energy* **2017**, *2*, 780.
[56] F. Sorgini, A. Mazzoni, L. Massari, R. Caliò, C. Galassi, S. L. Kukreja, E. Sinibaldi, M. C. Carrozza, C. M. Oddo, *Micromachines* **2017**, *8*, 270.
[57] Y. Su, X. Ping, K. J. Yu, J. W. Lee, J. A. Fan, B. Wang, M. Li, R. Li, D. V. Harburg, Y. Huang, *Adv. Mater.* **2017**, *29*, 1604989.
[58] R. Xu, J. W. Lee, T. Pan, S. Ma, J. Wang, J. H. Han, Y. Ma, J. A. Rogers, Y. Huang, *Adv. Funct. Mater.* **2017**, *27*, 1604545.
[59] K.-I. Jang, H. U. Chung, S. Xu, C. H. Lee, H. Luan, J. Jeong, H. Cheng, G.-T. Kim, S. Y. Han, J. W. Lee, *Nat. Commun.* **2015**, *6*, 6566.
[60] X. Chen, *Small Methods* **2017**, *1*, 1600029.
[61] F. Bossuyt, T. Vervust, J. Vanfleteren, *IEEE Trans. Compon. Packag. Manuf. Technol.* **2013**, *3*, 229.
[62] M. Gonzalez, F. Axisa, M. V. Bulcke, D. Brosteaux, B. Vandevelde, J. Vanfleteren, *Microelectron. Reliab.* **2008**, *48*, 825.
[63] Y.-Y. Hsu, M. Gonzalez, F. Bossuyt, F. Axisa, J. Vanfleteren, I. De Wolf, *J. Micromech. Microeng.* **2010**, *20*, 075036.
[64] M. L. Scarpello, D. Kurup, H. Rogier, D. V. Ginste, F. Axisa, J. Vanfleteren, W. Joseph, L. Martens, G. Vermeeren, *IEEE Trans. Antennas Propag.* **2011**, *59*, 3556.
[65] S. Xu, Y. Zhang, J. Cho, J. Lee, X. Huang, L. Jia, J. A. Fan, Y. Su, J. Su, H. Zhang, *Nat. Commun.* **2013**, *4*, 1543.
[66] S. Xu, Y. Zhang, L. Jia, K. E. Mathewson, K.-I. Jang, J. Kim, H. Fu, X. Huang, P. Chava, R. Wang, *Science* **2014**, *344*, 70.
[67] K.-I. Jang, K. Li, H. U. Chung, S. Xu, H. N. Jung, Y. Yang, J. W. Kwak, H. H. Jung, J. Song, C. Yang, *Nat. Commun.* **2017**, *8*, 15894.
[68] Y.-Y. Hsu, M. Gonzalez, F. Bossuyt, F. Axisa, J. Vanfleteren, I. De Wolf, *J. Mater. Res.* **2009**, *24*, 3573.
[69] Y.-Y. Hsu, M. Gonzalez, F. Bossuyt, F. Axisa, J. Vanfleteren, I. De Wolf, *Thin Solid Films* **2011**, *519*, 2225.
[70] D.-H. Kim, J. Song, W. M. Choi, H.-S. Kim, R.-H. Kim, Z. Liu, Y. Y. Huang, K.-C. Hwang, Y.-w. Zhang, J. A. Rogers, *Proc. Natl. Acad. Sci. USA* **2008**, *105*, 18675.
[71] S. P. Lacour, J. Jones, S. Wagner, T. Li, Z. Suo, *Proc. IEEE* **2005**, *93*, 1459.
[72] H. Lee, T. K. Choi, Y. B. Lee, H. R. Cho, R. Ghaffari, L. Wang, H. J. Choi, T. D. Chung, N. Lu, T. Hyeon, *Nat. Nanotechnol.* **2016**, *11*, 566.
[73] T. Li, Z. Suo, S. P. Lacour, S. Wagner, *J. Mater. Res.* **2005**, *20*, 3274.
[74] T. Chang, Y. Tanabe, C. C. Wojcik, A. C. Barksdale, S. Doshay, Z. Dong, H. Liu, M. Zhang, Y. Chen, Y. Su, *Adv. Funct. Mater.* **2017**, *27*, 1703059.

 © 2019 WILEY-VCH Verlag GmbH & Co. KGaA, Weinheim

[75] Y. H. Jung, H. Zhang, S. J. Cho, Z. Ma, *IEEE Trans. Electron Devices* **2017**, *64*, 1881.
[76] J. A. Fan, W.-H. Yeo, Y. Su, Y. Hattori, W. Lee, S.-Y. Jung, Y. Zhang, Z. Liu, H. Cheng, L. Falgout, *Nat. Commun.* **2014**, *5*, 3266.
[77] H. Fu, K. Nan, W. Bai, W. Huang, K. Bai, L. Lu, C. Zhou, Y. Liu, F. Liu, J. Wang, *Nat. Mater.* **2018**, *17*, 268.
[78] B. H. Kim, J. Lee, S. M. Won, Z. Xie, J.-K. Chang, Y. Yu, Y. K. Cho, H. Jang, J. Y. Jeong, Y. Lee, *ACS Nano* **2018**, *12*, 4164.
[79] Z. Liu, D. Qi, W. R. Leow, J. Yu, M. Xiloyannnis, L. Cappello, Y. Liu, B. Zhu, Y. Jiang, G. Chen, *Adv. Mater.* **2018**, *30*, 1707285.
[80] S. Xu, Z. Yan, K.-I. Jang, W. Huang, H. Fu, J. Kim, Z. Wei, M. Flavin, J. McCracken, R. Wang, *Science* **2015**, *347*, 154.
[81] Y.-H. Zhang, Y. Li, S.-Y. Fu, J. H. Xin, W. A. Daoud, L.-F. Li, *Polymer* **2005**, *46*, 8373.
[82] Y. Zhang, Z. Yan, K. Nan, D. Xiao, Y. Liu, H. Luan, H. Fu, X. Wang, Q. Yang, J. Wang, *Proc. Natl. Acad. Sci. USA* **2015**, *112*, 11757.
[83] Y. Zhang, F. Zhang, Z. Yan, Q. Ma, X. Li, Y. Huang, J. A. Rogers, *Nat. Rev. Mater.* **2017**, *2*, 17019.
[84] Y. Zhang, S. Wang, X. Li, J. A. Fan, S. Xu, Y. M. Song, K. J. Choi, W. H. Yeo, W. Lee, S. N. Nazaar, *Adv. Funct. Mater.* **2014**, *24*, 2028.

© 2019 WILEY-VCH Verlag GmbH & Co. KGaA, Weinheim